HHS Public Access

Author manuscript

*Free Radic Biol Med*. Author manuscript; available in PMC 2017 December 01.

Published in final edited form as:

*Free Radic Biol Med*. 2016 December ; 101: 367–377. doi:10.1016/j.freeradbiomed.2016.10.503.

# The tetrahydrobiopterin radical with high- and low-spin heme in neuronal nitric oxide synthase -- a new indicator of the extent of NOS coupling

**Matthew D. Krzyaniak**[a,1], **Alex A. Cruce**[a,2], **Preethi Vennam**[a], **Molly Lockart**[a], **Vladimir Berka**[b], **Ah-Lim Tsai**[b], and **Michael K. Bowman**[*,a]

[a]Department of Chemistry, The University of Alabama, Tuscaloosa, Alabama, 35487-0336 USA

[b]Division of Hematology, Department of Internal Medicine, University of Texas Health Science Center, Houston, Texas 77030 USA

## Abstract

Reaction intermediates trapped during the single-turnover reaction of the neuronal ferrous nitric oxide synthase oxygenase domain (Fe(II)nNOS$_{OX}$) show four EPR spectra of free radicals. Fully-coupled nNOS$_{OX}$ with cofactor (tetrahydrobiopterin, $BH_4$) and substrate (L-arginine) forms the typical $BH_4$ cation radical with an EPR spectrum ~4.0 mT wide and hyperfine tensors similar to reports for a biopterin cation radical in inducible NOS$_{OX}$ (iNOS$_{OX}$). With excess thiol, nNOSox lacking $BH_4$ and L-arg is known to produce superoxide. In contrast, we find that nNOS$_{OX}$ with $BH_4$ but no L-arg forms two radicals with rather different, fast (~ 250 μs at 5 K) and slower (~ 500 μs at 20 K), electron spin relaxation rates and a combined ~7.0 mT wide EPR spectrum. Rapid freeze-quench CW- and pulsed-EPR measurements are used to identify these radicals and their origin. These two species are the same radical with identical nuclear hyperfine couplings, but with spin-spin couplings to high-spin (4.0 mT component) or low-spin (7.0 mT component) Fe(III) heme. Uncoupled reactions of nNOS leave the enzyme in states that can be chemically reduced to sustain unregulated production of NO and reactive oxygen species in ischemia-reperfusion injury. The broad EPR signal is a convenient indicator of uncoupled nNOS reactions producing low-spin Fe(III) heme.

### Keywords

Nitric oxide synthase; Tetrahydrobiopterin radical; EPR; ENDOR; ESEEM

[*]To whom correspondence should be addressed. Phone: +1-(205)-348-7846 mkbowman@ua.edu.

[1]Present Addresses: Argonne-Northwestern Solar Energy Research (ANSER) Center, Northwestern University, 2190 Campus Drive, Evanston, IL 60208-3113 USA

[2]Department of Physics, Chemistry and Biology (IFM), Linköping University, Linköping, Sweden 581 83

## Introduction

Nitric oxide synthase (NOS) is a homodimeric, heme-containing, mono-oxygenase that produces nitric oxide (NO), a biomolecule important in a number of physiological and pathophysiological processes. The three NOS isoforms in mammals are: constitutive nNOS and eNOS, producing nanomolar amounts of NO for signaling; and inducible iNOS, producing micromolar amounts in the immune response. These isoforms share 50–60% sequence identity and are composed of a heme-containing oxygenase domain ($NOS_{OX}$) and a flavin-containing reductase domain linked by a calmodulin binding site. The three isoforms are expressed in different tissues and are regulated differently [1].

Each NOS isoform converts its L-arginine (L-arg) substrate to NO using a tetrahydrobiopterin cofactor ($BH_4$, Scheme 1) in a series of tightly-coupled reactions. In several common pathological conditions, the reactions become uncoupled, producing reactive oxygen species (ROS): superoxide and/or hydrogen peroxide in place of NO [2–7]. For example, during ischemia caused by stroke or infarct, tissues become highly reduced because cytochrome *c* oxidase can no longer dispose of electrons to $O_2$. Consequently, $NOS_{OX}$ may be reduced to its substrate-free Fe(II) heme state; a state rigorously avoided under normal conditions. When reperfusion restores $O_2$ to the tissue, the incoming $O_2$ reacts with the reduced state of NOS to produce ROS [8] and may continue to do so as long as the tissue can reduce $NOS_{OX}$. Repeated cycles of unregulated reduction and ROS production could cause major tissue damage, the so-called reperfusion injury.

NOS behaves like a self-sufficient P450-like enzyme. NO is formed in a pair of sequential mono-oxygenase reaction cycles in $NOS_{OX}$. In the first cycle, Scheme 2, L-arg is hydroxylated to produce N-hydroxy-L-arginine using $O_2$ and two reducing equivalents. One reducing equivalent comes from NADPH in the reductase domain but the other electron, in contrast to classical P450 enzymes, comes from the $BH_4$ bound in $NOS_{OX}$. The second oxygenation cycle uses an additional reducing equivalent and another $O_2$ to convert N-hydroxy-L-arginine into NO and L-citrulline, and still uses $BH_4$ for a $2^{nd}$ reducing equivalent.

The first reaction cycle is well characterized under normal conditions [10–13]. It starts in step (1) when L-arg binds to oxidized $NOS_{OX}$ and displaces the water serving as the sixth, axial ligand of the low-spin, Fe(III) heme, raising the heme redox potential. The heme becomes high-spin and is rapidly reduced in (2) to Fe(II) heme by the reductase domain and immediately binds $O_2$. The resulting (Fe(II) heme-$O_2$) is rapidly reduced in (3) by the bound $BH_4$ cofactor. If reduction by $BH_4$ is delayed, the (Fe(II) heme-$O_2$) can decompose to produce superoxide or hydrogen peroxide, due to the very hydrophilic heme distal pocket. Otherwise, the normal reduction step produces an intermediate often described as a hybrid, indicated by square brackets, between (Fe(II) heme-$O_2^-$) and (Fe(III) heme-$O_2^{2-}$). This intermediate may react directly with substrate or it may eliminate water to form a ferryl heme (Fe(IV) heme=O) and then transfer its oxygen to the L-arg substrate in (4) [11]. The $NOS_{OX}$ is left containing N-hydroxy-L-arginine and Fe(III) heme, poised to start the second reaction cycle. The $BH_4$ cofactor is a free radical, but is soon reduced. The strict sequence of these reactions is enforced under normal conditions by several tactics that prevent heme

reduction in the absence of substrate. Rapid freeze-quench (RFQ) electron paramagnetic resonance (EPR) spectroscopy in iNOS identified the $BH_4$ radical through $^{15}N$ labelling at the N5 position [14]. Subsequent EPR studies found the same $BH_4$ radical in all isoforms [15–18] as the $BH_4$ radical cation [15] and we find no new evidence disputing that assignment.

Crystal structures of $NOS_{OX}$ show $BH_4$ bound near the heme along the homodimer interface [19–21]. The $BH_4$ is sandwiched between two aromatic amino acids and makes three hydrogen bonds with the heme propionate group (from N3, from N2 and, via a bridging water, from O4 of the $BH_4$), Figure 1. The hydrogen bonds provide an electron transfer path from $BH_4$ to the heme and they stabilize the $BH_4$ radical cation. However, $BH_4$ is too far from the (Fe(IV) heme=O) for the activated oxygen to attack and modify it. Yet, $BH_4$ does form a triad with heme and L-arg in an extended, hydrogen-bonded network that rigidifies the active site scaffolding and helps regulate the axial water ligation controlling the high/low-spin and redox states of the heme. A mutual enhancement of the binding of each element of the triad also guides the relative orientation of $O_2$ and L-arg which is crucial for ensuring the high fidelity of the monooxygenation reactions.

Reactions of $nNOS_{OX}$ that occur under pathological conditions are much less studied or understood although they can have a major impact on human health, for example, in ischemia-reperfusion injury. We have used single-turnover, RFQ EPR after mixing pre-reduced nNOSox (Fe(II)$NOS_{OX}$) with $O_2$ to study radical species during the first cycle of NOS catalysis under pathological conditions [8, 22, 23]. We found the expected $BH_4$ radical cation when both $BH_4$ and L-arg were bound to $NOS_{OX}$ as Fe(II)$NOS_{OX}$(+$BH_4$, +L-arg). In Fe(II)$NOS_{OX}$(−$BH_4$, ±L-arg), we saw the (Fe(II) heme-$O_2$) decompose to produce mainly superoxide [8, 22, 23]. However, a new EPR signal appears in all three NOS isoforms when Fe(II)$NOS_{OX}$(+$BH_4$, −L-arg) reacts with $O_2$ [8]. This radical bears some resemblance to the $BH_4$ radical cation seen in normal turnover, but its EPR spectrum has more extensive wings, greater asymmetry, and, in $nNOS_{OX}$ and $eNOS_{OX}$, a larger peak-to-peak linewidth. This altered spectrum is accompanied by changes in the reaction kinetics. The new spectrum appears as (Fe(II) heme-$O_2$) decays, but it appears three times faster than the rate of normal electron transfer from $BH_4$ to (Fe(II) heme-$O_2$) with L-arg present, and more than seven times faster than the rate of decomposition of (Fe(II) heme-$O_2$) to superoxide when $BH_4$ is absent [8]. It is important to identify this new EPR spectrum and to determine the products of reduced $NOS_{OX}$ when L-arg is depleted because NOS has the potential to repeatedly cycle with $O_2$ in highly-reducing tissues to produce ROS.

In this study, we examine resting $nNOS_{OX}$ and the states produced by reactions of $O_2$ with reduced $nNOS_{OX}$ containing $BH_4$ in the presence or absence of L-arg in RFQ samples denoted $nNOS_{FQ}$(+$BH_4$, ±L-arg). We seek to determine the products and whether they have the potential to support continued turnover of the enzyme. The RFQ samples are carefully prepared under single turnover conditions which means that they cannot go beyond the first cycle of the NOS reaction. The pre-reduced $nNOS_{OX}$ lacks the reductase domain and so, after one turnover, there is no reductant available to support further reaction. Thus the RFQ traps the enzyme somewhere within or at the completion of the first cycle. We focus on characterizing the new free radical spectrum observed in $nNOS_{FQ}$(+$BH_4$, −L-arg) and

contrasting it with the $BH_4$ radical cation seen during normal turnover. We find that the new radical is derived from $BH_4$ and is spin-coupled to a low-spin heme from the first turnover of nNOS.

## Materials and Methods

### Protein Expression and Purification

Protein expression and purification of the oxidase domain of rat brain nNOS was performed as previously described [23]. Freshly-purified $nNOS_{OX}$ (200 μM) in buffer (50 mM HEPES, 0.1mM NaCl, 1mM DTT, 10% glycerol, pH 7.5) was reconstituted overnight with $BH_4$ (500 μM) and/or L-arg (2 mM) under anaerobic conditions. Excess $BH_4$ was removed by a 10-DG desalting column (Bio-Rad) equilibrated with buffer in the presence or absence of 2 mM L-arg. The eluted protein was concentrated with a Centriprep-50K concentrator to 200 μM and stored at 77 K.

### Pulsed EPR Sample Preparation

The sample preparation procedure was similar to that for previous RFQ experiments [23, 24]. The appropriate frozen protein stock solution of 200 μM ferric heme Fe(III)$nNOS_{OX}$(+$BH_4$, ±2 mM L-arg) was thawed and then reduced to Fe(II)$nNOS_{OX}$ by anaerobic titration with a minimal excess of dithionite in a glass titrator (with 2 mm cuvette attached). Completion of the reduction was determined spectrophotometrically as a shift of the heme Soret peak to 414 nm, a marker for Fe(II)$nNOS_{OX}$. The RFQ was performed inside an anaerobic chamber using an Update Instruments Inc. System 1000 freeze-quench apparatus. Equal volumes of Fe(II)$nNOS_{OX}$ solution and air-saturated buffer (plus 2 mM L-arg, as appropriate) were rapidly mixed and freeze-quenched into prechilled isopentane (−140 °C) after reaction for 125 ms, which maximizes the amount of trapped radicals while allowing the activated oxygen-heme complexes to form and react/decay. The resulting frozen particles were packed into 4 mm o.d. quartz EPR tubes and stored in liquid nitrogen. Resting $nNOS_{OX}$(+$BH_4$, ±2 mM L-arg) samples were made by freezing the appropriate stock solution, as isolated, in 4 mm o.d. EPR tubes.

### CW-EPR

The CW EPR spectra were measured on an ELEXSYS E540 X-band spectrometer (Bruker-Biospin, Billerica, MA) with an ER 4102 ST resonator using 100 kHz magnetic field modulation. Spectra were measured at 77 K in a liquid-nitrogen quartz insertion dewar and at lower temperatures with a Bruker ER 4112 HV helium flow cryostat. Care was taken to avoid microwave power saturation or modulation broadening in the CW EPR spectra that are reported or analyzed.

### Pulsed EPR

Pulsed EPR measurements were made at X-band with a nominal microwave frequency of 9.76 GHz using an ELEXSYS E680 EPR spectrometer equipped with a Flexline ER 4118 CF cryostat and ER 4118X-MD4 electron nuclear double resonance (ENDOR) resonator. Echo-detected EPR (ED-EPR) spectra were measured from the integrated echo intensity as a function of the applied magnetic field. The spin echo was generated using a two-pulse spin

echo sequence, π/2-τ-π-τ-*echo*, where τ is the time delay between pulses and π/2 or π denote microwave pulses, nominally 16 or 32 ns in length, that rotate electron spins through angles of π/2 or π, respectively. The *echo* indicates the signal whose intensity is measured [25]. A four-step phase cycle, +(0,0), -(π,0), +(0,π), -(π, π), was used for suppression of unwanted signals and baseline correction [26]. The spin-lattice relaxation rate of the high-spin heme signal was measured by saturation recovery [25].

Mims ENDOR spectra were measured using an ENI A-500 RF power amplifier and the Mims ENDOR pulse sequence, π/2-τ-π/2-T- π/2-τ-*echo* with a 10 μs RF π-pulse applied during the delay time T and the four-step phase cycle for the stimulated echo [25, 27, 28]. The Mims ENDOR spectra are presented as the absolute ENDOR effect which is the change in echo intensity with RF on and off resonance divided by the echo intensity with the RF off resonance. We obtain excellent reproducibility in the magnitude of the ENDOR effect with Mims ENDOR. Spectra can be compared quantitatively to detect changes in hyperfine couplings or isotopic content without the scaling or shifting needed for spectra obtained by the Davies ENDOR sequence. In addition, Mims ENDOR can be simulated by *de facto* standard software like EasySpin [29, 30] without arbitrary corrections (as in Davies ENDOR) for pulse-width artifacts [31, 32]. Two-dimensional hyperfine sublevel correlation (HYSCORE) spectra were measured with a 4-pulse microwave sequence, π/2-τ-π/2-$t_1$-π-$t_2$-π/2-τ-*echo* with a four-step phase cycle, where τ, $t_1$, and $t_2$ indicate independently-incremented delays that produce a two-dimensional dataset [27, 28, 33, 34]. HYSCORE correlates ENDOR transitions of the same nucleus in different electron spin states and can resolve overlapping ENDOR transitions. The HYSCORE spectra were measured in the vicinity $g_z$ to determine hyperfine tensors that are not coaxial with the g-tensor [28, 35, 36].

## Spectral Simulation and Processing

The value of the zero field splitting, D, of the high-spin heme was determined from the relative EPR susceptibility and from the Orbach-Aminov spin-lattice relaxation rates. The relative spin susceptibility was determined by integrating the low-field, first-derivative peak [37, 38]. Those values were fit by the theoretical equation for S=5/2, of $T^{-1}(1+\exp(-2D/k_BT)+\exp(-6D/k_BT))^{-1}$ to determine D. The spin-lattice relaxation rate of the high-spin signal from saturation recovery measurements [25] was fit between 3.5–7 K by $(\exp(-2D/k_BT)-1)^{-1}$. The Orbach-Aminov process involves thermal excitation to higher energy levels [39], in this case, from the $m_S=\pm1/2$ to the $m_S=\pm3/2$ levels of the high-spin heme, revealing the value of D.

CW spectra were simulated and analyzed using EasySpin [29, 30] to obtain *g*-values, *g*-strain, E/D, D-strain and the fraction of each distinct species in the sample, using the value of D=8.2 $cm^{-1}$ determined independently. The measurement temperature was explicitly included in the simulations to account for thermal depopulation of spin levels in the high-spin species. The pulsed EPR spectra were processed using the Xepr software package (Bruker-Biospin, Billerica, MA) or with custom MatLab (MathWorks) scripts. Analysis of coupled anisotropic spins follows the methods developed previously [40–42].

## Results

The oxidized resting $nNOS_{OX}$ samples with or without L-arg (±L-arg), denoted $nNOS_{OX}(-BH_4, +L\text{-arg})$ or $nNOS_{OX}(-BH_4, -L\text{-arg})$, respectively, are stable and unreactive, but establish important spectroscopic benchmarks for the heme. The RFQ samples of pre-reduced oxidase domain with $BH_4$ ±L-arg, denoted $nNOS_{FQ}(+BH_4, +L\text{-arg})$, and $nNOS_{FQ}(+BH_4, -L\text{-arg})$, were prepared by mixing with $O_2$ to maximize the amount of $BH_4$ radical cation. Like all RFQ samples, they are a snapshot of the reacting solution and may contain multiple states along one or more reaction pathways, including small amounts of unreacted, but EPR silent, reduced nNOS.

### The Heme

**CW-EPR—**The CW-EPR spectra of all four states were measured at 10 K, Figure 2. The CW-EPR spectra contain a mixture of high-spin and low-spin oxidized heme. The high-spin (S=5/2) heme produces spectral lines near 87 mT (g~7.9), 160 mT (g~3.8) and 375 mT (g~1.8). These three lines are transitions within the $m_S=\pm½$ effective electron spin manifold. Another set of lines near 278 mT (g~2.5), 296 mT (g~2.3) and 355 mT (g~1.9) arise from the low-spin (S=1/2) heme and are assigned to principal values of the g-tensor, $g_z$, $g_y$, $g_x$, respectively, Table 1. Prominent organic radical signals in $nNOS_{FQ}(+BH_4, \pm L\text{-arg})$ near 336 mT have been blanked in Figure 2 because their signals are severely distorted by large microwave power and modulation amplitude. The free radical spectra are considered below.

Simulation of the high-spin Fe(III) heme emphasized two critical features of EPR spectrum. One is the shape and intensity of the low-field peak at g~7.9 because the integral of this feature is directly proportional to the number of spins [37] which is important for determining the relative yields of high-spin and low-spin forms in the sample. The other critical feature is the position (but not the shape) of the peaks near g~3.8 and ~7.9 which are sensitive the value of E/D [43]. This strategy gives accurate relative numbers of spins, while using a simplified spin Hamiltonian for rapid calculations. However, the simulated g~4.3 signal near 115 mT (transitions between the $m_S=3/2$ levels), Figure 2 (b–c), is too sharp and prominent while the simulated g~3.8 signal near 160 mT is too broad.

The heme spectra, Figure 2, show several overlapping peaks at the $g_x$ and $g_z$ features of the low-spin heme and at the feature near 160 mT from high-spin heme. These overlapping peaks arise from spectrally-distinct forms of the NOS. Low-spin heme is generally considered to arise from $NOS_{OX}$ with an axial water ligand on the heme and the high-spin heme from NOS with five-coordinate heme. However, local structural variations in the environment of the heme, e.g., in its hydrogen bonding network, within the active site can produce g-factor shifts of the magnitude seen here [36, 44]. The heme spectra in every sample can be fit with a mixture of the same five heme spectral components: two high-spin hemes and three low-spin hemes, Figure 2. Thus in each sample, there are local structural variations around the heme so that the spectrum is not a combination of just one high-spin and one low-spin heme spectra. In addition, different samples do not have spectral components different from those of other samples. This is a strong indication that the heme in each $nNOS_{OX}$ sample has a mix of the same five local environments but in different proportions. The single-turnover reactions do not produce any new local environment for the

heme. The EPR parameters of the five heme spectral components and their relative amounts are listed in Table 1.

The fits indicate that addition of primary substrate, L-arg, converts $nNOS_{OX}$ from >90% low-spin heme to >70% high-spin heme. The L-arg displaces the axial water ligand of the heme, converting the six-coordinate, low-spin heme to five-coordinate, high-spin heme. This change in spin state is seen in the increased amplitude of the high-spin peaks at 87 mT (g~7.9) and 160 mT (g~3.8) relative to those of the low-spin heme. The high-spin peak at 160 mT, Figure 2b, has a poorly-resolved splitting that could only be reproduced using two nearly-axial high-spin species with E/D parameters of 0.081 and 0.071. The zero field splitting, D, was too large to determine from the CW-EPR spectrum at X-band. The value of D was determined from relative EPR susceptibility between 5–35 K and from the spin-lattice relaxation rate between 3.5–7 K where the Orbach-Aminov process dominates [39]. Both measurements indicate a value for D of 8.2 $cm^{-1}$, Figure 3.

The RFQ samples start fully reduced and EPR silent, but addition of oxygenated buffer initiates reactions that generate paramagnetic species which are trapped upon freezing. The heme spectrum of $nNOS_{FQ}$(+$BH_4$, +L-arg), Figure 2c, is >95% high-spin heme and that of $nNOS_{FQ}$(+$BH_4$, −L-arg) is a ~5:2 mixture of low-spin and high-spin heme, Figure 2d. The high-spin heme has the same EPR spectral parameters, Table 1, and spin-lattice relaxation rates, Figure 3 Inset, in all samples independent of whether the $BH_4$ radical is present or of whether L-arg (or presumably N-hydroxy-L-arginine) occupies the active site.

**HYSCORE—**The ligation of the low-spin heme was probed using HYSCORE spectroscopy. Distinct arcs from $^1H$ having significant hyperfine couplings to the low-spin heme were seen in HYSCORE spectra of resting $nNOS_{OX}$(−$BH_4$, −L-arg) and $nNOS_{FQ}$(+$BH_4$, −L-arg), Figure 4. The positions of the arcs correlate the two ENDOR frequencies of a $^1H$ nucleus in the $m_S$=±½ electron spin manifolds. The arcs are displaced slightly toward the upper right corner of the spectrum by second-order shifts, resolving signals that overlap in an ENDOR spectrum [28, 45]. The prominent outer arcs shifted furthest toward the upper right-hand corner are from the axial water ligand of the heme while the other prominent pair are from the β-$CH_2$ group of the cysteine that is the proximal axial ligand in NOS and cytochrome P450 [28, 35, 44, 46]. Simulation of the water arcs gives a dipolar hyperfine interaction corresponding to a distance of 0.25±0.01 nm between the hydrogen and the heme iron and an angle of ~37° between the $g_z$ axis of the heme and the vector connecting the iron and the hydrogen. This distance and orientation is in excellent agreement with the axial water ligand expected in NOS and observed in P450 [35, 44, 46]. The lower pair of $^1H$ arcs corresponds to a distance of 0.33 nm and an angle of ~47°, consistent with a β-$^1H$ of the proximal cysteine ligand [44]. The same arcs from water, but with much more noise, are still seen in $nNOS_{FQ}$(−$BH_4$, +L-arg) where the same low-spin heme spectra are seen in lower yields, Figure 2 and Table 1. The similar spectra indicate that the axial water ligand has the same conformation after one turnover as it has in the oxidized resting state without L-arg.

## The Radical

**CW-EPR—**CW-EPR spectra of RFQ samples in $H_2O$ and $D_2O$ at 77 K show strong free radical signals, Figure 5. The free radical with poorly-resolved hyperfine structure in $nNOS_{FQ}$(+$BH_4$, +L-arg), Figure 5a, is consistent with previous results [23]. The lineshape is the combined result of hyperfine interactions with nitrogen and hydrogen nuclear spins in and around the radicals, of g-factor anisotropy which is minor at X-band, and magnetic interactions with nearby paramagnetic centers such as the heme. Deuteration of the buffer sharpens the spectrum and decreases the number of hyperfine lines, Figure 5b, suggesting a strong hyperfine interaction with one exchangeable hydrogen. The remainder of the hyperfine structure can be fit using a strong coupling with a nitrogen and a strong coupling with a non-exchangeable hydrogen, similar to previous results on pterin radicals in NOS [14, 15]. The CW-EPR spectrum of nNOSox(+$BH_4$, −L-arg) labeled with $^{15}N$ at N5 of $BH_4$ loses some of the structure at the center of radical spectrum, Figure 5e, and can only be simulated if the large nitrogen hyperfine coupling is from N5.

The RFQ reaction without L-arg results in a broad radical signal, Figure 5c–e, for $nNOS_{FQ}$(+$BH_4$, −L-arg). This broad radical signal has hyperfine structure at the center (334 – 339 mT) similar to the $BH_4$ radical spectrum. However the wings of the spectrum extend more than 5 mT beyond the edges of the $BH_4$ radical spectrum in $nNOS_{FQ}$(+$BH_4$, +L-arg). Deuteration of the buffer simplifies the hyperfine structure at the center, Figure 5d, but without the increased resolution noted in $nNOS_{FQ}$(+$BH_4$, +L-arg). The wings extend quite a bit less from the center than those in Figure 5c, yet noticeably farther than those in the $nNOS_{FQ}$(+$BH_4$, +L-arg) samples. The radical signal in $nNOS_{FQ}$(+$BH_4$, −L-arg) shows a strong hyperfine interaction with an exchangeable hydrogen but possible contributions from the residual narrow $BH_4$ radical spectrum complicate interpretation of the new, broad spectrum. Isotopic labelling with $^{15}N$ at the N5 position results in a radical spectrum in $nNOS_{FQ}$(+$BH_4$, −L-arg), Figure 5e, with less-prominent hyperfine structure at the center. That structure is matched by EasySpin simulations taking into account the isotopic substitution, Figure 5e. The $^{15}N$ labelling has little effect on the overall extent of the radical spectrum in $nNOS_{FQ}$(+$BH_4$, −L-arg), which is expected because $^{14}N$ and $^{15}N$ make essentially identical contributions to the second moment of the EPR spectrum.

Pulsed EPR measurements were undertaken to identify the new broad radical signal in $nNOS_{FQ}$(+$BH_4$, −L-arg). Relaxation measurements were used to distinguish overlapping spectra in both types of RFQ samples while ENDOR and electron spin echo envelope modulation (ESEEM) spectra were used to characterize weak hyperfine couplings.

**Electron Spin Echo—**Two-pulse spin echo measurements show a striking difference between the free radical signals in the RFQ samples. The spin echo intensity in $nNOS_{FQ}$(+$BH_4$, +L-arg), Figure 6c, has a strong temperature dependence; much stronger than the 1/T expected from the Boltzmann factor for a free radical. The spin echo signal is not detected above 9 K because of rapid phase memory relaxation, consistent with results by Stoll et al. on iNOS [15]. The spin-lattice relaxation is exceptionally fast for an organic free radical; the spin-lattice relaxation time, $T_{1e}$, is ~250 μs at 5 K. The free radical signal in $nNOS_{FQ}$(+$BH_4$, −L-arg) behaves somewhat differently, Figure 6d. A portion of the spin echo

signal behaves exactly like the signal in $nNOS_{FQ}(+BH_4, +L\text{-arg})$ - rapid relaxation and strong temperature dependence. However, a slower-relaxing component persists at higher temperatures.

ED-EPR spectra of the two species can be measured by exploiting their dependence on temperature and pulse repetition rate. After spins are excited by the microwave pulses to produce an echo, the spins must have time for spin-lattice relaxation to occur before another echo signal can be produced. At a 2 kHz pulse repetition rate, the slow-relaxing radical in $nNOS_{FQ}(+BH_4, -L\text{-arg})$ does not have time to completely recover below 20 K before the next set of pulses occurs. Consequently, below 10 K only the fast-relaxing radical signal is seen at the 2 kHz repetition rate. However, at a 0.1 kHz repetition rate, both types of signals recover during the delay between pulse sequences and both are observed below 10 K. Above 10 K only the spectrum of the slow-relaxing signal can be observed because the signal from the fast-relaxing radical has decayed within the deadtime of the spectrometer.

The ED-EPR spectrum of the fast-relaxing radical in $nNOS_{FQ}(+BH_4, +L\text{-arg})$ at 4 K, Figure 6a, is fairly symmetric, consistent with the CW-EPR spectrum and the fast-relaxing component in $nNOS_{FQ}(+BH_4, -L\text{-arg})$. This spectrum disappears above 10 K because of its rapid echo decay. However, the ED-EPR spectrum of the slow-relaxing radical is seen well above 13 K in $nNOS_{FQ}(+BH_4, -L\text{-arg})$ at a 0.1 kHz repetition rate, Figure 6b. The slow-relaxing spectrum is asymmetric and considerably broader than that of the fast-relaxing signal. Its wings are consistent with the CW-EPR spectrum of $nNOS_{FQ}(+BH_4, -L\text{-arg})$ considering that the ED-EPR spectra have some additional broadening from the measurement conditions [25, 47].

The rapid phase memory relaxation and spin-lattice relaxation of the radical in $nNOS_{FQ}(+BH_4, +L\text{-arg})$ suggests that this radical is close to a very fast-relaxing paramagnetic center. The only other paramagnetic species seen in the CW-EPR spectrum, Figure 2c, in comparable amounts is the high-spin heme. Its $T1_e$ has a very strong temperature dependence in that temperature range, Figure 3 Inset, consistent with it being the partner of the fast-relaxing radical.

The saturation of the slow-relaxing radical signal below 20 K at a 2 kHz repetition rate indicates $T_{1e}$ is ~500 μs at 20 K. Such a value is rather short for a typical organic π-radical and suggests that this radical also is interacting with a paramagnetic center. But the disparate relaxation properties of the two free radical signals indicate differences either in their chemical identities; in the properties of paramagnetic centers with which they interact; or in the strengths of that interaction.

**ENDOR—**We used Mims ENDOR to measure the weak hyperfine interactions of the two radical species and to determine if the radicals were chemically different. The strongest hyperfine couplings (for example, to N5, and to hydrogens on N5 and C6, in $nNOS_{FQ}(+BH_4, +L\text{-arg})$), can be determined by fitting the CW-EPR spectra. But ENDOR probes the unpaired spin distribution in the rest of the radical and readily detects changes in hydrogen bonding or radical conformation.

Mims ENDOR spectra of the individual radical species were obtained by exploiting the differences in their relaxation. Mims $^{1}$H ENDOR spectra in $H_2O$ and $D_2O$, Figure 7, were obtained for $nNOS_{FQ}$(+$BH_4$, +L-arg) at 4 K and for $nNOS_{FQ}$(+$BH_4$, −L-arg) at 10 K, where only the narrow, fast-relaxing radical and the new, broad, slow-relaxing radical, respectively, are observed. The slight asymmetry in all the spectra seems to be a characteristic of our resonator/RF amplifier combination, so simulated spectra were scaled to match the high-frequency side. The strong peak in the center of each spectrum is the 'matrix' ENDOR line from a multitude of weakly-coupled $^{1}$H in the solvent and protein. The matrix ENDOR peak decreases significantly in samples prepared in $D_2O$. Flanking the matrix line are additional peaks from $^{1}$H in the radicals.

The ENDOR spectra of the two free radicals are essentially the same. They can be quantitatively fit using the same sets of hyperfine interactions. Two hydrogens, one exchangeable and the other non-exchangeable, are readily identified by ENDOR, Figure 7. H/D exchange in $D_2O$ buffer causes a notable decrease in ENDOR intensity between 12.0–17.5 MHz from exchangeable $^{1}$H in the radical and simulations give a hyperfine tensor of [2.5, 5.0, 6.5] MHz in the axis system of Stoll et al. [15]. The non-exchangeable hydrogen appears as a broad feature extending from ~8–12 MHz and ~18–22 MHz in all spectra. In the ENDOR spectrum with $\tau$=132 ns, the 'blindspots' [48] at 11.2 and 18.7 MHz sit nearly at the center of this feature. Simulations indicate a non-exchangeable $^{1}$H with a hyperfine tensor of [4.0, 14.0, 8.0] MHz. Three-pulse ESEEM measurements on the radicals in the RFQ samples give identical modulation typical of $^{14}$N in a nitrogen-based $\pi$ radical. The hyperfine couplings determined here for nNOS, Table 2, are similar to those reported by Stoll et al. [15] for the $BH_4$ radical cation in iNOS but differ in the tentative assignment of $^{1}$H at C7 and N8.

The ENDOR and ESEEM spectra are virtually identical for the narrow, fast-relaxing $BH_4$ radicals in $nNOS_{FQ}$(+$BH_4$, ±L-arg) and for the broad, slow-relaxing radical in $nNOS_{FQ}$(+$BH_4$, −L-arg). This indicates that the hyperfine couplings in the ENDOR and ESEEM are the same in both types of radical. The similar amplitudes of the ENDOR effect and the similar ESEEM depths mean that all radicals contributing to the broad signal have the same ENDOR spectrum. All the available experimental data for large and small $^{1}$H and $^{14}$N hyperfine couplings coincide; yet the slow-relaxing radical has significant, additional broadening. The additional broadening cannot be due to new, large hyperfine interactions. The broadening is so large that the unpaired spin would need to be localized at a single atom in the radical and not delocalized in a $\pi$ radical. Such a major redistribution of unpaired spin density in the radical makes it inconceivable that the ENDOR and ESEEM spectra would remain the same. The free radical signals in all RFQ samples must arise from the $BH_4$ radical cation with the same hyperfine couplings and the additional broadening in the slow-relaxing radical cannot be caused by hyperfine interactions.

**Spin-Spin Interactions—**We argued above that spin-spin interactions with the fast-relaxing, high-spin heme are responsible for the rapid spin-lattice relaxation and the rapid spin echo decay of the narrow radical signal. That spin-spin interaction could also broaden the narrow radical signal although rapid relaxation of the heme would attenuate the broadening by dynamic averaging caused by changes in the direction and amplitude of the

heme's spin projection. In $nNOS_{FQ}$(+$BH_4$, −L-arg), about ¾ of the heme(III) is in the low-spin form and could be the source of the broadening and of the slower, but still enhanced, relaxation of the slow-relaxing radical signal. The residual fast-relaxing radical signal in that sample would arise from $BH_4$ cation radicals interacting with the remaining ~1/4 of the high-spin heme whose EPR spectral properties, Table 1, and $T_{1e}$, Figure 3, are the same in both RFQ samples.

Simulation of the spin-coupled CW-EPR spectrum of the $BH_4$ radical cation interacting with the low-spin heme is straightforward. The comparatively slow spin-lattice relaxation of the low-spin heme allows its spin dynamics to be neglected below 77 K and the EPR parameters of the heme and the radical are known. We modelled the broad free radical spectra, Figure 5c–e, as a sum of i) the residual fast-relaxing $BH_4$ radical cation spectrum simulated in Figure 5a–b, plus ii) the same radical with an additional coupling to the low-spin heme (taking into account its anisotropic g-tensor). Good fits, Figure 5c–e, were obtained with an exchange coupling, J~104 MHz (for exchange interaction defined as +J $S_1S_2$), and an electron-electron dipole interaction of 40 MHz directed approximately along the $g_y$ axis of the heme. The fits of the free radical spectra in $nNOS_{FQ}$(+$BH_4$, −L-arg) successfully reproduce the overall width, the poorly-resolved structure, the lineshape changes in $D_2O$ or with $^{15}N$, and the slight asymmetry. The fits are sums of spectra from the narrow radical and the broad radical. The fit spectrum in Figure 5c is 70±10% broad radical, comparable to the 77% low-spin heme in that sample, Table 1 and Figure 2d. The low-spin heme yield is somewhat less in the deuterated samples with correspondingly lower contributions from the broad radical spectrum, ~15% in Figure 5d. Consequently, the wings of the broad signal extend nearly as far from the center of the spectrum in Figure 5d, but are less prominent because of the low amplitude relative to the intense contribution from the narrow radical at the center of the spectrum.

Spin coupling between the $BH_4$ radical and the low-spin heme is required to successfully simulate the radical CW-EPR spectrum. Yet coupling to the high-spin heme is not needed for good spectral simulations at 77 K because spin-lattice relaxation is much faster for high-spin heme than for low-spin heme. The faster spin-lattice relaxation modulates the interactions of the heme with the radical spins rapidly enough at 77 K to 'average' most of the broadening from the spin-spin interaction, producing a spectrum that is largely determined by the hyperfine coupling and, at higher fields, g-factor anisotropy [15], not by interactions with the high-spin heme. Broadening of the narrow radical signal as the temperature is lowered was reported by Stoll et al. in iNOS [15] and is observed here in $nNOS_{FQ}$(+$BH_4$, +L-arg) between 10–40 K, Figure 8. It clearly shows broadening of the signal from the radical at low temperatures where the high-spin heme has a spin-lattice relaxation rate on the order of tens of MHz. That broadening diminishes at higher temperatures as the high-spin heme relaxation becomes much faster and is not apparent at 40 K and above. Spin coupling among the five unpaired electrons of the high-spin heme may modify and even weaken the spin-spin interactions with the radical, but the rapid spin-lattice relaxation above 40 K is a decisive factor for the width of the narrow, free-radical EPR spectrum when high-spin heme is present.

In summary, the rapid spin relaxation of the high-spin heme has a major effect on the spin relaxation of the radical, but not its EPR spectrum, while the low-spin heme has a lesser effect on relaxation of the radical but a major effect on its spectrum. Thus, we assign the narrow, fast-relaxing radical signal in $nNOS_{FQ}$(+$BH_4$, ±L-arg) to the $BH_4$ radical cation in a $nNOS_{OX}$ subunit containing high-spin heme (III); and the broad, slow-relaxing radical in $nNOS_{FQ}$(+$BH_4$, −L-arg) to the same $BH_4$ radical cation in those $nNOS_{OX}$ subunits containing low-spin heme(III).

## Discussion

### Reactivity of $BH_4$ plays a decisive role in NOS behavior

Conventional P450 enzymes that metabolize hydrophobic xenobiotic compounds employ a range of intermediate electron donors. However, NOS uses only $BH_4$ as the immediate source of the 2nd electron in both of its mono-oxygenase catalytic cycles to metabolize very polar amino acid substrates. Only in the presence of $BH_4$ is NOS able to achieve optimal coupling of its reactions to produce NO rather than ROS/RNS. The presence or absence of $BH_4$ plays a decisive role in the coupling of NOS reactions and determines the role of NOS in normal physiology versus pathology. Our EPR/ENDOR/ESSEM study is the only one to address the structure/activity relationship of NOS under all conditions of presence or absence of $BH_4$ and L-arg.

### The Heme after a Single Turnover

The EPR parameters of the heme(III) reflect the ligand field and environment around the heme. The presence or absence of a sixth, axial ligand determines whether the heme is high spin or low spin. Even subtle differences in protein conformation, hydrogen bonding to the ligands of the iron or nearby charges, produce slight shifts in g-values and peak positions in the EPR spectrum. We found five distinct heme(III) EPR spectra which are present in each sample, but in different ratios, Table 1. Earlier spin-counting experiments in this system show that the EPR signals account for nearly all of the heme in each sample [23] with little or no residual EPR-silent Fe(II).

There are no new heme(III) species after a single turnover with $BH_4$ present, so $nNOS_{OX}$(+$BH_4$, ±L-arg) returns to a state very much like its starting state. The binding of $BH_4$ or L-arg does not alter any of the five heme spectra, only the quasi-equilibrium between them. Even the hydrogen bonding between $BH_4$ and one of the heme propionate groups seems to have no impact on the heme's EPR spectral properties.

### The $BH_4$ cation radical after a Single Turnover

The free radical spectra and spin relaxation rates observed after a single turnover with and without L-arg are significantly different, which gave the initial impression of different radicals or different chemical forms of the $BH_4$ radical. However, the ENDOR, ESEEM and the CW EPR consistently indicate the same hyperfine couplings across the entire radical spectrum and the same unpaired spin distribution in both radicals. The EPR spectra in both types of samples can be simulated by taking into account the differences in electron spin-spin interactions with high-spin versus low-spin heme(III). The broad radical spectrum has

~100 MHz electron exchange interaction and 40 MHz dipole-dipole interaction with low-spin heme. These interaction energies amount to ~0.04 J/mol and ~0.02 J/mol, respectively; which are chemically insignificant yet spectroscopically prominent. The corresponding interactions of the high-spin heme fail to produce most of their potential broadening of the radical CW EPR spectrum at 77 K because of the dynamic averaging of the interactions by rapid spin relaxation of the high-spin heme.

Assignment of the free radical spectrum to the same $BH_4$ cation radical interacting with high-and low-spin heme(III) is consistent with the two half-saturation power ($P_{1/2}$) values of 37 and 14.7 mW obtained for $nNOS_{FQ}$(+$BH_4$, −L-arg) radical [23]. The former value is close to the $P_{1/2}$ of 27 mW in $nNOS_{FQ}$(+$BH_4$, +L-arg), and both $P_{1/2}$ values are much smaller than that for the superoxide radical, ~100 mW, in samples without $BH_4$ [23]. The first $P_{1/2}$ probably comes from radicals interacting with high-spin heme(III) and the second $P_{1/2}$ from chemically-identical radicals interacting with the slow-relaxing low-spin heme(III). This interpretation also would apply to $eNOS_{OX}$ [22]. A single $P_{1/2}$ of 37 mW was reported in $iNOS_{FQ}$(+$BH_4$, −L-arg) [8] but close examination of the published spectra shows that the wings of that spectrum saturate more easily than the center. An estimate at the wider wing trough gives $P_{1/2}$ ~7 mW and makes the RFQ EPR results from all three NOS isoforms consistent.

## Single-Turnover Reactions with both $BH_4$ and L-arg

The samples started as oxidized $nNOS_{OX}$(+$BH_4$, +L-arg), presumably with L-arg displacing the axial water ligand of the resting state to give the high-spin heme(III) state, Figure 1. This state was chemically reduced to five-coordinate heme(II) for the start of the RFQ process. After a single turnover, the $nNOS_{FQ}$(+$BH_4$, +L-arg) samples are again in a high-spin, heme(III) state, presumably near the start of the second turn of the NOS cycle. The L-arg has been converted to N-hydroxy-L-arginine, but still displaces the axial water ligand, and the $BH_4$ has been converted to its cation radical. If highly-reduced tissue reduces both the $BH_4$ and the high-spin heme(III) of $nNOS_{OX}$, the second cycle of the NOS reaction could proceed with unregulated producton of NO and heme(III)$nNOS_{OX}$ (+$BH_4$, −L-arg).

## Single-Turnover Reactions without L-arg

The oxidized $nNOS_{OX}$(+$BH_4$, −L-arg) samples start mainly in the low-spin heme(III) state with an axial water ligand, Figure 1. This state was chemically reduced to heme(II), presumably in some equilibrium between the five- and six-coordinate forms, at the start of the RFQ process. After reacting, the $nNOS_{FQ}$(+$BH_4$, −L-arg) samples have a $BH_4$ cation radical and a heme(III), ~1/4 high spin and ~3/4 low spin. Simulations of the CW EPR spectra and spin-counting [23] gave similar ~75% yields for heme(III) and radicals. Each radical interacts with a heme(III), and no other paramagnetic products are seen. In particular, no superoxide is produced by fresh $nNOS_{OX}$(+$BH_4$, −L-arg) [23]. It is very significant that the reactions have consumed $O_2$ and two reducing equivalents, one from $BH_4$ and the other from heme(II), in the same protein. There are two reasonable reactions that may have occurred. One possibility is that the (Fe(II) heme-$O_2^-$)/(Fe(III) heme-$O_2^{2-}$) or the (Fe(IV) heme=O) oxygenates some residue of $nNOS_{OX}$, damaging the protein. This is unlikely because the same sample can be redox cycled another round with essentially the same

reactivity. The more likely reaction is the transformation of (Fe(II) heme-$O_2^-$)/(Fe(III) heme-$O_2^{2-}$) into $H_2O_2$ and Fe(III) heme. The NOS heme pocket is designed for chemical conversion of a very hydrophilic substrate and this greatly facilitates rapid decomposition of the (Fe(II) heme-$O_2^-$)/(Fe(III) heme-$O_2^{2-}$) into $H_2O_2$. In contrast, typical P450 enzymes have hydrophobic substrates and produce $H_2O_2$ slowly. $H_2O_2$ is a known product in stopped-flow studies of this reaction in iNOS [8], but we have not made similar studies in nNOS. However, quantitative $H_2O_2$ formation in uncoupled nNOS has been reported using diacetyldeuteroheme-substituted horseradish peroxidase as a trapping agent [49].

The heme(III) after a single turnover is an intriguing mixture of five-coordinate, high-spin and six-coordinate, low-spin states. The HYSCORE and CW EPR spectra find that the sixth, axial ligand in the low-spin heme is the same water in the same positions and same orientations as in the resting state of the enzyme. But why is the water ligand absent in 24% of the $nNOS_{FQ}$(+$BH_4$, −L-arg)? A simple explanation would be that the heme(III) has reached equilibrium with the aqueous solvent and 24% of the heme(III) lacks the water ligand. The resting $nNOS_{OX}$(−$BH_4$, −L-arg) certainly is at equilibrium with solvent yet only 9% of it lacks the water ligand. The $BH_4$ binds well away from the water ligand position and it would not be expected to have a direct effect on the state of heme(III). However, the triad of $BH_4$, L-arg and heme do mutually enhance one another to rigidify the heme pocket via the H-bond network indicated in Figure 1 [8, 22, 23, 50]. Apparently, the H-bonding also propagates a slight stabilization of the high-spin species by $BH_4$ in nNOS (Table 1) and eNOS, inferred from the optical blue shift of the Soret band when $BH_4$ binds [22, 23].

On the other hand, the water ligand in $nNOS_{FQ}$(+$BH_4$, −L-arg) might not reach equilibrium with solvent during freeze quenching. In that case, the original water ligand of the reduced heme(II) might remain in the active site and return to the heme(III) so that the products reflect the initial reduced $nNOS_{OX}$(+$BH_4$, −L-arg). Clearly, more work is needed to determine the full significance of the spin state distribution, but the low-spin heme product and the broad radical spectrum serve as indicators of uncoupled NOS reactions.

## nNOS in Highly-Reduced Tissues – Biological Implications

A single turnover of $nNOS_{OX}$(+$BH_4$, ±L-arg) in these studies generates the $BH_4$ cation radical and heme(III) in the protein. If $BH_4$ and heme(II) are regenerated in highly-reduced tissue, the $nNOS_{OX}$ domain of nNOS would react with any $O_2$ present and cycle again. The $nNOS_{OX}$ domain would produce $H_2O_2$, N-hydroxy-L-arginine, NO and L-citrulline until $O_2$ or the ability of the tissue to reduce the $nNOS_{OX}$ domain, directly or via the reductase domain, is exhausted. Under these same conditions, $nNOS_{OX}$(−$BH_4$, ±L-arg) produces superoxide and heme(III) [8, 23] and should also repeatedly turnover. The other isoforms of NOS appear to share these abilities. Whenever $O_2$ becomes available during reperfusion of highly-reduced tissues all NOS isoforms could be diverted into unregulated production of NO, ROS, or even peroxynitrite, depending on the availability of $BH_4$ and L-arg, independent of the ROS production by the reductase domain of NOS.

Chemical reduction of the $nNOS_{OX}$ domain in the absence of its $BH_4$ cofactor and/or its natural substrates generates superoxide or $H_2O_2$ from $O_2$. Moreover, any oxidase domains of nNOS that are chemically reduced in highly-reduced tissues during infarct or ischemia

escape the normal regulation provided by the reductase domain and calmodulin/$Ca^{+2}$. Thus, even when $BH_4$ and L-arg are present in reduced tissues, the normal regulation of NOS activity, which involves tight control of its enzymatic reduction, would be circumvented and would allow unregulated NO production and signaling errors.

## Conclusion

The CW- and pulsed-EPR, ENDOR and spin echo studies of the multiple EPR spectra of free radicals formed during the reaction of Fe(II)nNOS$_{OX}$ with oxygen converge on a simple interpretation. Previous studies showed that in the absence of $BH_4$, nNOS$_{OX}$(−$BH_4$,±L-arg) generates mainly superoxide radicals. In the presence of $BH_4$, nNOS$_{OX}$(+$BH_4$,±L-arg) forms the cation radical of $BH_4$. In the present work, we show that its spin-exchange and dipolar interactions with the Fe(III)heme in high-spin or low-spin state produce the well-known ~4.0 mT wide spectrum of the $BH_4$ cation radical or the broad ~7.0 mT wide spectrum of the $BH_4$ cation radical, respectively. Identification of these radical products reveal the possible reactions that can occur in uncoupled nNOS and the broad radical spectrum provides a clear indication of uncoupled NOS turnover. The ability to distinguish between the various product states of NOS provides a foundation for future mechanistic deciphering of the network of reactions catalyzed by nNOS and the other NOS isozymes in several pathological states.

## Acknowledgments

This work was supported by National Institutes of Health [grant number HL095820].

## Abbreviations

| | |
|---|---|
| **arg** | arginine |
| **$BH_4$** | tetrahydrobiopterin |
| **CW** | continuous wave |
| **ED-EPR** | echo-detected EPR |
| **ENDOR** | electron nuclear double resonance |
| **EPR** | electron paramagnetic resonance, also known as ESR or electron spin resonance |
| **HYSCORE** | hyperfine sublevel correlation spectroscopy |
| **mT** | milliTesla |
| **NADPH** | reduced nicotinamide adenine dinucleotide phosphate |
| **NO** | nitric oxide |
| **NOS** | nitric oxide synthase |
| **eNOS** | endothelial nitric oxide synthase |

| | |
|---|---|
| **iNOS** | inducible nitric oxide synthase |
| **nNOS** | neuronal nitric oxide synthase |
| **$NOS_{FQ}$** | freeze quenched NOS |
| **$NOS_{OX}$** | resting oxygenase domain of NOS |
| **RFQ** | rapid freeze quench |
| **T** | Tesla |
| **$T_M$** | phase memory time or the characteristic time for decay of the two-pulse electron spin echo |
| **$T_1$** | spin-lattice relaxation time |

## REFERENCES


1. Wei CC, Crane BR, Stuehr DJ. Tetrahydrobiopterin radical enzymology. Chem. Rev. 2003; 103(6): 2365–2383. [PubMed: 12797834]
2. Pou S, Pou WS, Bredt DS, Snyder SH, Rosen GM. Generation of Superoxide by Purified Brain Nitric-Oxide Synthase. J. Biol. Chem. 1992; 267(34):24173–24176. [PubMed: 1280257]
3. Xia Y, Roman LJ, Masters BSS, Zweier JL. Inducible nitric-oxide synthase generates superoxide from the reductase domain. J. Biol. Chem. 1998; 273(35):22635–22639. [PubMed: 9712892]
4. Xia Y, Tsai AL, Berka V, Zweier JL. Superoxide generation from endothelial nitric-oxide synthase - A $Ca^{2+}$/calmodulin-dependent and tetrahydrobiopterin regulatory process. J. Biol. Chem. 1998; 273(40):25804–25808. [PubMed: 9748253]
5. Xia Y, Dawson VL, Dawson TM, Snyder SH, Zweier JL. Nitric oxide synthase generates superoxide and nitric oxide in arginine-depleted cells leading to peroxynitrite-mediated cellular injury. Proc. Natl. Acad. Sci. USA. 1996; 93(13):6770–6774. [PubMed: 8692893]
6. Vasquez-Vivar J, Kalyanaraman B, Martasek P, Hogg N, Masters BSS, Karoui H, Tordo P, Pritchard KA. Superoxide generation by endothelial nitric oxide synthase: The influence of cofactors. Proc. Natl. Acad. Sci. USA. 1998; 95(16):9220–9225. [PubMed: 9689061]
7. Heinzel B, John M, Klatt P, Bohme E, Mayer B. $Ca^{2+}$/Calmodulin-Dependent Formation of Hydrogen-Peroxide by Brain Nitric-Oxide Synthase. Biochem. J. 1992; 281:627–630. [PubMed: 1371384]
8. Berka V, Liu W, Wu G, Tsai A-L. Comparison of oxygen-induced radical intermediates in iNOS oxygenase domain with those from nNOS and eNOS. J. Inorg. Biochem. 2014; 139(0):93–105. [PubMed: 25016313]
9. Blumberg, WE., Peisach, J. Low-Spin Compounds of Heme Proteins. In: Dessy, R.Dillard, J., Taylor, L., editors. Bioinorganic Chemistry. Washington, D. C.: American Chemical Society; 1971. p. 271-291.
10. Feng C. Mechanism of nitric oxide synthase regulation: Electron transfer and interdomain interactions. Coord. Chem. Rev. 2012; 256(3–4):393–411. [PubMed: 22523434]
11. Daff S. NO synthase: Structures and mechanisms. Nitric Oxide-Biology and Chemistry. 2010; 23(1):1–11. [PubMed: 20303412]
12. Stuehr DJ, Santolini J, Wang ZQ, Wei CC, Adak S. Update on mechanism and catalytic regulation in the NO synthases. J. Biol. Chem. 2004; 279(35):36167–36170. [PubMed: 15133020]
13. Feng CJ, Chen L, Li WB, Elmore BO, Fan WH, Sun X. Dissecting regulation mechanism of the FMN to heme interdomain electron transfer in nitric oxide synthases. J. Inorg. Biochem. 2014; 130:130–140. [PubMed: 24084585]

14. Hurshman AR, Krebs C, Edmondson DE, Huynh BH, Marletta MA. Formation of a pterin radical in the reaction of the heme domain of inducible nitric oxide synthase with oxygen. Biochemistry. 1999; 38(48):15689–15696. [PubMed: 10625434]
15. Stoll S, NejatyJahromy Y, Woodward JJ, Ozarowski A, Marletta MA, Britt RD. Nitric oxide synthase stabilizes the tetrahydrobiopterin cofactor radical by controlling its protonation state. J. Am. Chem. Soc. 2010; 132(33):11812–11823. [PubMed: 20669954]
16. Wei CC, Wang ZQ, Tejero J, Yang YP, Hemann C, Hille R, Stuehr DJ. Catalytic reduction of a tetrahydrobiopterin radical within nitric-oxide synthase. J. Biol. Chem. 2008; 283(17):11734–11742. [PubMed: 18283102]
17. Brunel A, Santolini J, Dorlet P. Electron Paramagnetic Resonance Characterization of Tetrahydrobiopterin Radical Formation in Bacterial Nitric Oxide Synthase Compared to Mammalian Nitric Oxide Synthase. Biophys. J. 2012; 103(1):109–117. [PubMed: 22828337]
18. Tejero J, Stuehr D. Tetrahydrobiopterin in nitric oxide synthase. IUBMB Life. 2013; 65(4):358–365. [PubMed: 23441062]
19. Li HY, Igarashi J, Jamal J, Yang WP, Poulos TL. Structural studies of constitutive nitric oxide synthases with diatomic ligands bound. J. Biol. Inorg. Chem. 2006; 11(6):753–768. [PubMed: 16804678]
20. Raman CS, Li HY, Martasek P, Babu BR, Griffith OW, Masters BSS, Poulos TL. Implications for isoform-selective inhibitor design derived from the binding mode of bulky isothioureas to the heme domain of endothelial nitric-oxide synthase. J. Biol. Chem. 2001; 276(28):26486–26491. [PubMed: 11331290]
21. Fischmann TO, Hruza A, Niu XD, Fossetta JD, Lunn CA, Dolphin E, Prongay AJ, Reichert P, Lundell DJ, Narula SK, Weber PC. Structural characterization of nitric oxide synthase isoforms reveals striking active-site conservation. Nat. Struct. Biol. 1999; 6(3):233–242. [PubMed: 10074942]
22. Berka V, Wu G, Yeh HC, Palmer G, Tsai AL. Three different oxygen-induced radical species in endothelial nitric-oxide synthase oxygenase domain under regulation by L-arginine and tetrahydrobiopterin. J. Biol. Chem. 2004; 279(31):32243–32251. [PubMed: 15166218]
23. Berka V, Wang LH, Tsai AL. Oxygen-induced radical intermediates in the nNOS oxygenase domain regulated by L-arginine, tetrahydrobiopterin, and thiol. Biochemistry. 2008; 47(1):405–420. [PubMed: 18052254]
24. Du M, Yeh HC, Berka V, Wang LH, Tsai AL. Redox properties of human endothelial nitric-oxide synthase oxygenase and reductase domains purified from yeast expression system. J. Biol. Chem. 2003; 278(8):6002–6011. [PubMed: 12480940]
25. Bowman, MK. Pulsed Electron Paramagnetic Resonance. In: Brustalon, M., Giamello, E., editors. Electron Paramagnetic Resonance - A Practitioner's Toolkit. Hoboken: John Wiley & Sons; 2009. p. 159-194.
26. Bowman, MK. Fourier Transform Electron Spin Resonance. In: Kevan, L., Bowman, MK., editors. Modern Pulsed and Continuous Electron Spin Resonance. New York: Wiley; 1990. p. 1-42.
27. Dikanov SA, Xun LY, Karpiel AB, Tyryshkin AM, Bowman MK. Orientationally-Selected Two-Dimensional ESEEM Spectroscopy of the Rieske-Type Iron-Sulfur Cluster in 2,4,5-Trichlorophenoxyacetate Monooxygenase from *Burkholderia cepacia* AC1100. J. Am. Chem. Soc. 1996; 118(35):8408–8416.
28. Cruce, AA., Lockart, M., Bowman, MK. Pulsed EPR in the Study of Drug Binding in Cytochrome P450 and NOS. In: Qin, PZ., Warncke, K., editors. Methods Enzymol. Academic Press; 2015. p. 311-340.
29. Stoll S, Britt RD. General and efficient simulation of pulse EPR spectra. Phys. Chem. Chem. Phys. 2009; 11(31):6614–6625. [PubMed: 19639136]
30. Stoll S, Schweiger A. EasySpin, a Comprehensive Software Package for Spectral Simulation and Analysis in EPR. J. Magn. Reson. 2006; 178(1):42–55. [PubMed: 16188474]
31. Doan PE, Fan CL, Davoust CE, Hoffman BM. A Simple Method for Hyperfine-Selective Heteronuclear Pulsed Endor Via Proton Suppression. J. Magn. Reson. 1991; 95(1):196–200.
32. Fan CL, Doan PE, Davoust CE, Hoffman BM. Quantitative Studies of Davies Pulsed Endor. J. Magn. Reson. 1992; 98(1):62–72.

33. Höfer P, Grupp A, Nebenfuehr H, Mehring M. Hyperfine sublevel correlation (HYSCORE) spectroscopy: a 2D ESR investigation of the squaric acid radical. Chem. Phys. Lett. 1986; 132:279.
34. Gemperle C, Aebli G, Schweiger A, Ernst RR. Phase Cycling in Pulse Epr. J. Magn. Reson. 1990; 88(2):241–256.
35. Conner KP, Schimpf AM, Cruce AA, McLean KJ, Munro AW, Frank DJ, Krzyaniak MD, Ortiz de Montellano P, Bowman MK, Atkins WM. Strength of Axial Water Ligation in Substrate-Free Cytochrome P450s Is Isoform Dependent. Biochemistry. 2014; 53(9):1428–1434. [PubMed: 24576089]
36. Conner KP, Cruce AA, Krzyaniak MD, Schimpf AM, Frank DJ, Ortiz de Montellano P, Atkins WM, Bowman MK. Drug Modulation of Water-Heme Interactions in Low-Spin P450 Complexes of CYP2C9d and CYP125A1. Biochemistry. 2015; 54(5):1198–1207. [PubMed: 25591012]
37. Aasa R, Vanngard T. Epr Signal Intensity and Powder Shapes - Re-Examination. J. Magn. Reson. 1975; 19(3):308–315.
38. Galli C, MacArthur R, Abu-Soud HM, Clark P, Stuehr DJ, Brudvig GW. EPR Spectroscopic Characterization of Neuronal NO Synthase. Biochemistry. 1996; 35(8):2804–2810. [PubMed: 8611587]
39. Bowman, MK., Kevan, L. Electron Spin-Lattice Relaxation in Nonionic Solids. In: Kevan, L., Schwartz, RN., editors. Time Domain Electron Spin Resonance. New York: Wiley; 1979. p. 67-105.
40. Vennam PR, Fisher N, Krzyaniak MD, Kramer DM, Bowman MK. A Caged, Destabilized, Free Radical Intermediate in the Q-Cycle. ChemBioChem. 2013; 14(14):1745–1753. [PubMed: 24009094]
41. Maryasov AG, Bowman MK. Spin Dynamics of Paramagnetic Centers with Anisotropic g Tensor and Spin of 1/2. J. Magn. Reson. 2012; 221(0):69–75. [PubMed: 22743542]
42. Maryasov AG, Bowman MK. Bloch equations for anisotropic paramagnetic centers with spin of 1/2. J. Magn. Reson. 2013; 233:80–86. [PubMed: 23786888]
43. Pilbrow JR. Effective G-Values for S = 3/2 and S = 5/2. J. Magn. Reson. 1978; 31(3):479–490.
44. Conner KP, Vennam P, Woods CM, Krzyaniak MD, Bowman MK, Atkins WM. 1,2,3-Triazole-Heme Interactions in Cytochrome P450: Functionally Competent Triazole-Water-Heme Complexes. Biochemistry. 2012; 51(32):6441–6457. [PubMed: 22809252]
45. Dikanov SA, Bowman MK. Cross-Peak Lineshape of Two-Dimensional ESEEM Spectra in Disordered S=1/2, I=1/2 Spin System. J. Magn. Reson., Ser A. 1995; 116:125–128.
46. Roberts AG, Cheesman MJ, Primak A, Bowman MK, Atkins WM, Rettie AE. Intramolecular Heme Ligation of the Cytochrome P450 2C9 R108H Mutant Demonstrates Pronounced Conformational Flexibility of the B-C Loop Region: Implications for Substrate Binding. Biochemistry. 2010; 49(40):8700–8708. [PubMed: 20815369]
47. Bowman MK, Krzyaniak MD, Cruce AA, Weber RT. Skew projection of echo-detected EPR spectra for increased sensitivity and resolution. J. Magn. Reson. 2013; 231(0):117–125. [PubMed: 23644351]
48. Tay-Agbozo SS, Krzyaniak MD, Bowman MK, Street S, Kispert LD. DFT and ENDOR Study of Bixin Radical Cations and Neutral Radicals on Silica-Alumina. J. Phys. Chem. B. 2015; 119(24): 7170–7179. [PubMed: 25333911]
49. Gao YT, Panda SP, Roman LJ, Martasek P, Ishimura Y, Masters BSS. Oxygen metabolism by neuronal nitric-oxide synthase. J. Biol. Chem. 2007; 282(11):7921–7929. [PubMed: 17229730]
50. Berka V, Tsai A-L. Characterization of Interactions among the Heme Center, Tetrahydrobiopterin, and L-Arginine Binding Sites of Ferric eNOS using Imidazole, Cyanide, and Nitric Oxide as Probes. Biochemistry. 2000; 39(31):9373–9383. [PubMed: 10924132]

## Highlights

- $BH_4$ radical cation is produced by nNOS with or without substrate
- Spin interactions with heme(III) enhance spin relaxation
- Spin interactions with heme(III) broaden the EPR signal of the $BH_4$ radical
- $BH_4$ plays a decisive role in the tight coupling of reactions in NOS
- Uncoupled NOS reactions can sustain unregulated production of reactive oxygen species

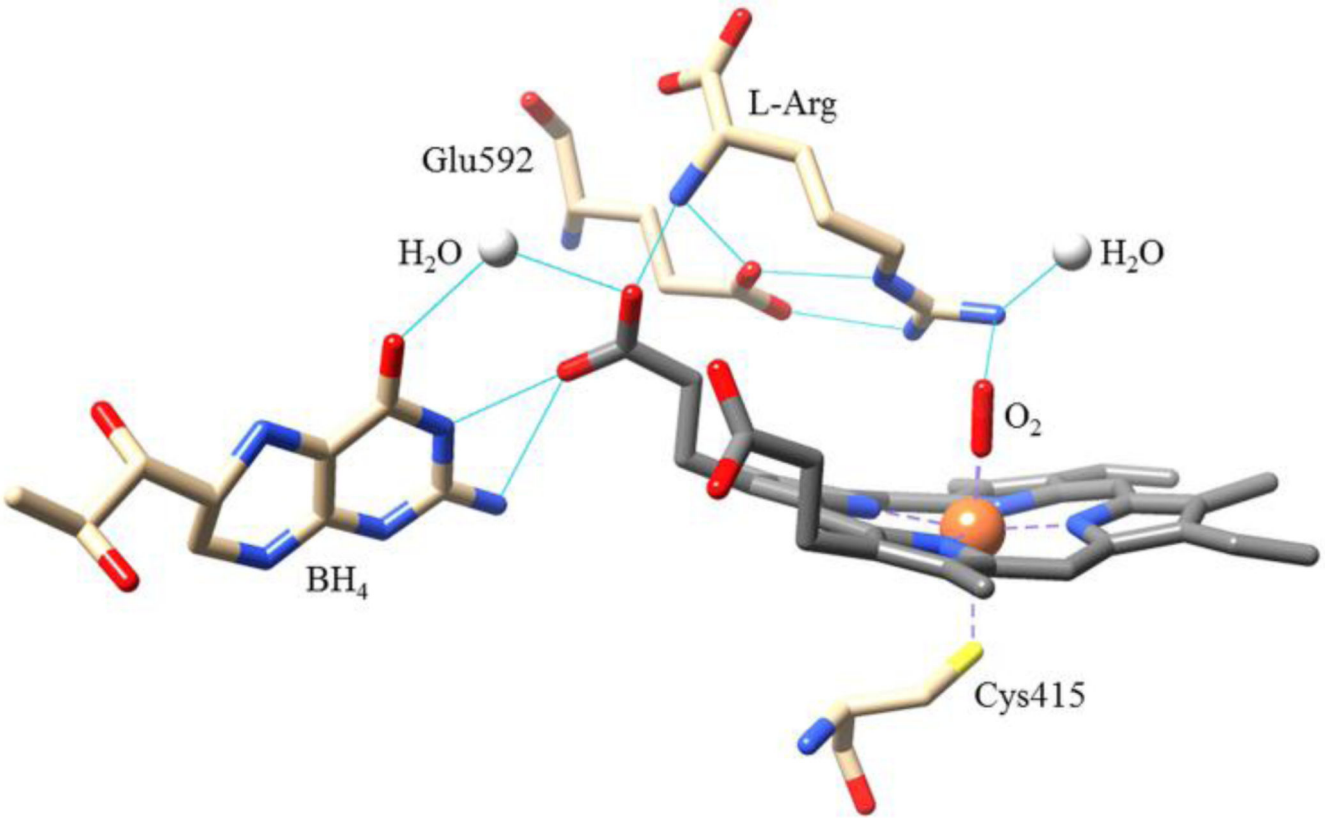


**Figure 1.**

Hydrogen-bonding among the "triad" of heme, $BH_4$ and L-arg. This network of bonds rigidifies the heme pocket scaffolding and regulates the heme spin-state changes caused by water ligation to the Fe(III). The $O_2$ bound to the heme is poised to attack the L-arg substrate. Adapted from the 1.85 Å resolution crystal structure of nNOSox, PDB: 2G6M.

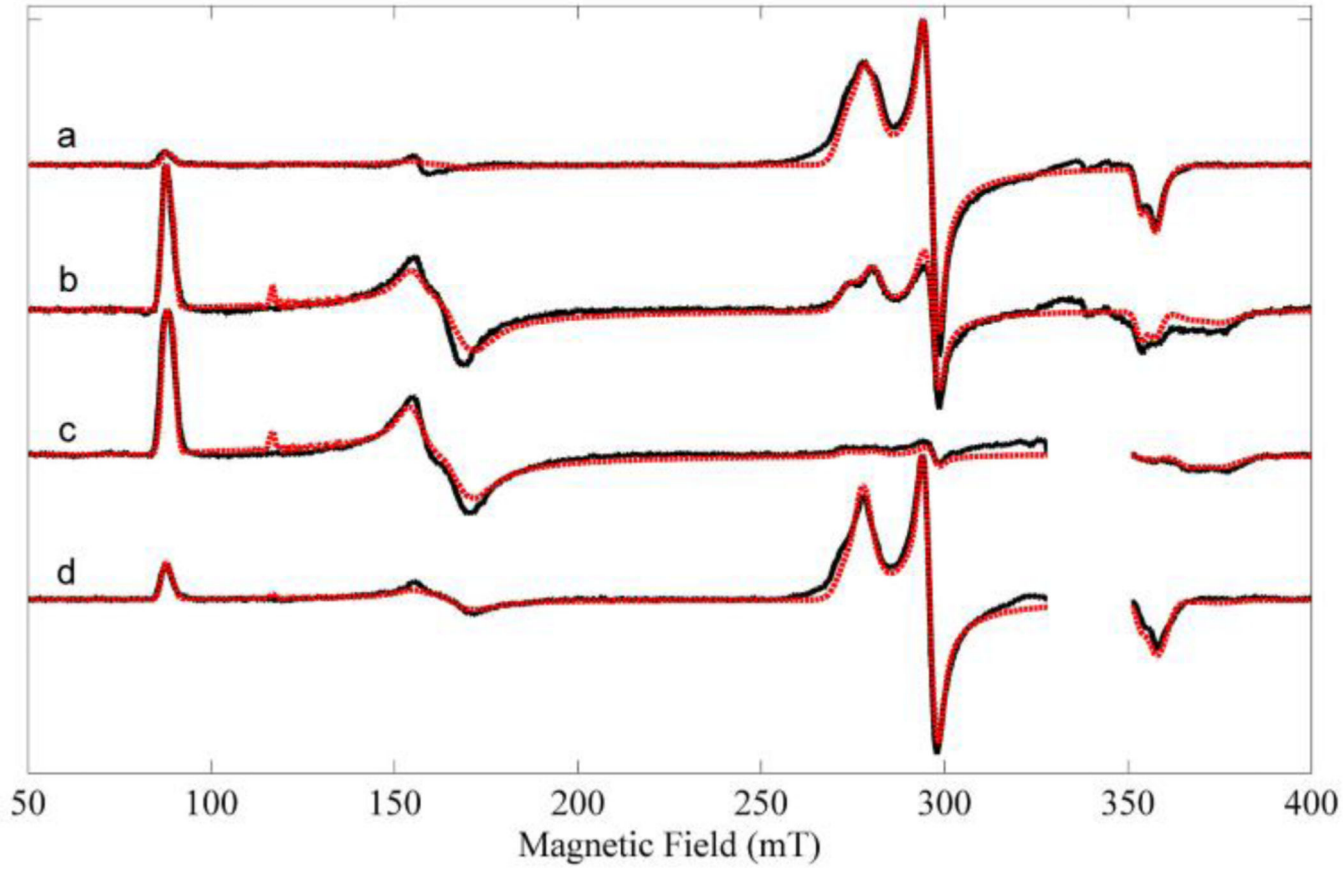


**Figure 2.**

Experimental and simulated CW-EPR spectra. (a) $nNOS_{OX}(-BH_4, -L\text{-arg})$, (b) $nNOS_{OX}(-BH_4, +L\text{-arg})$, (c) $nNOS_{FQ}(+BH_4, +L\text{-arg})$, and (d) $nNOS_{FQ}(+BH_4, -L\text{-arg})$. The black lines are experimental spectra and the red are simulations using the parameters in Table 1. The CW-EPR spectra were measured at 10 K using: microwave frequency, 9.46 GHz; microwave power, 0.21 mW; field modulation amplitude, 2 mT at 100 kHz. The region of strong signals from $BH_4$ radicals are blanked out in (c–d).

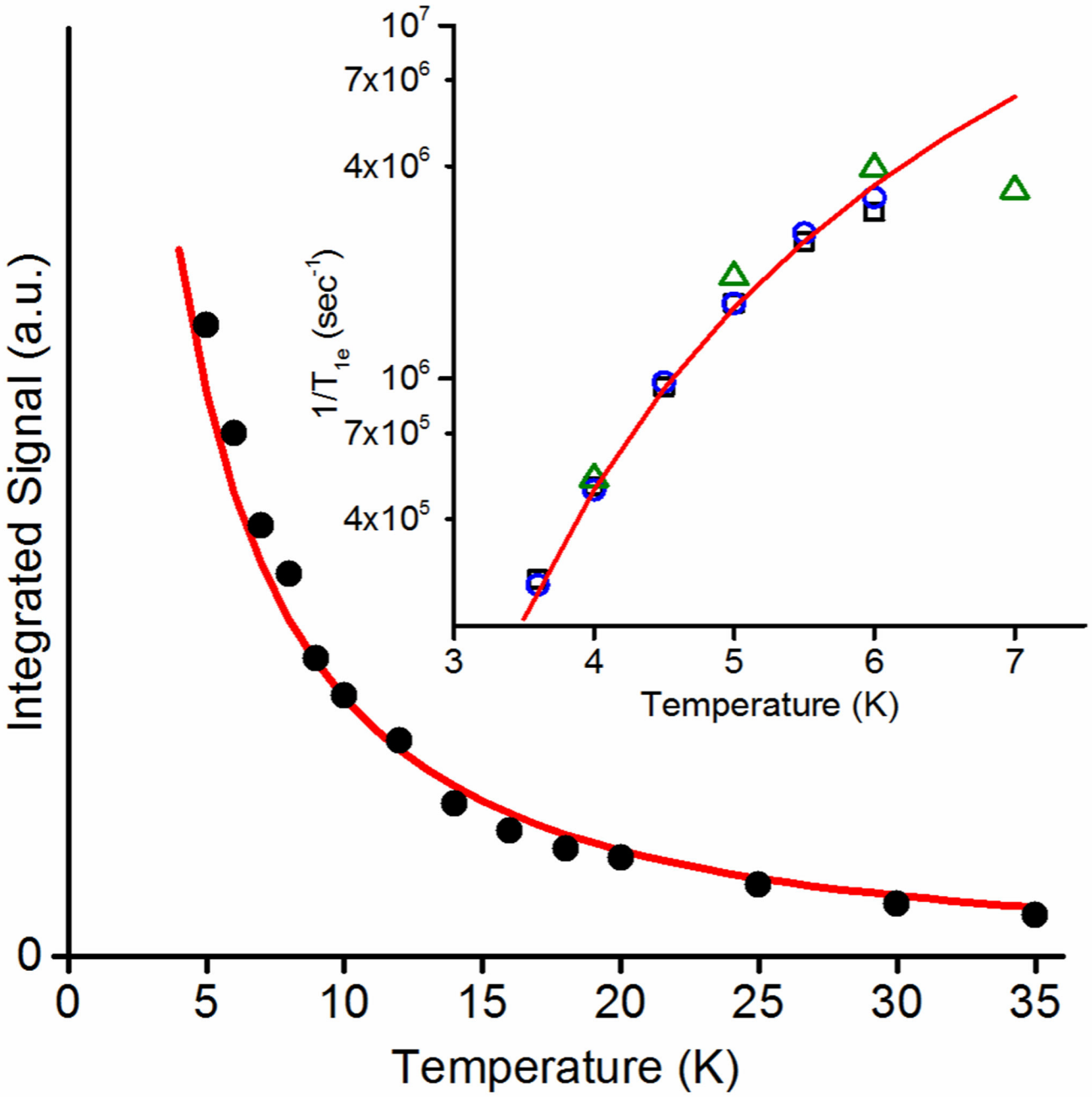


**Figure 3.**

Determination of the value of D. The integrated intensity of the CW-EPR peak of $nNOS_{FQ}$(+$BH_4$, +L-arg) near g~7.9 (filled black circles) is plotted versus temperature with the calculated fit of $T^{-1}(1+\exp(-2D/k_BT)+\exp(-6D/k_BT))^{-1}$, for D=8.2 $cm^{-1}$ (red line). Inset: Temperature dependence of the measured $T_{1e}$ of high-spin heme(III) (open black squares: $nNOS_{FQ}$(+$BH_4$, −L-arg), open blue circles: $nNOS_{FQ}$(+$BH_4$, +L-arg), open green triangles: $nNOS_{OX}$(−$BH_4$, +L-arg)) with the fit (solid red line) for an Orbach-Aminov relaxation process, $(\exp(-2D/k_BT)-1)^{-1}$, for D=8.2 $cm^{-1}$.

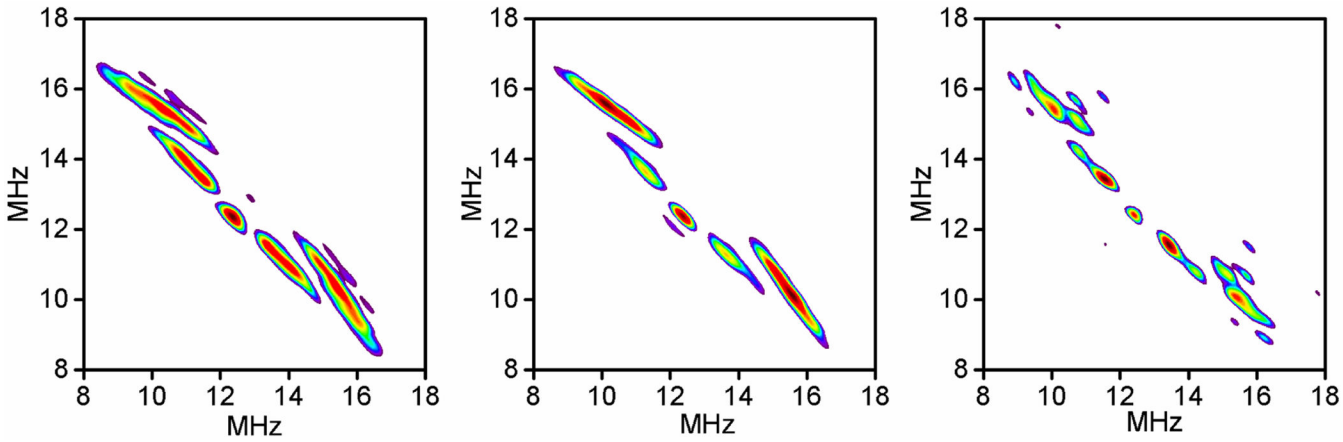


**Figure 4.**

The $^{1}H$ region of HYSCORE spectra at 10 K. Measurements near $g_z$ at g=2.40 (290 mT) with microwave frequency ~973 GHz and **τ**=160 ns. **Left**: resting $nNOS_OX(-BH_4, -L\text{-arg})$, **Center**: $nNOS_{FQ}(+BH_4, -L\text{-arg})$, and **Right**: $nNOS_{OX}(-BH_4, +L\text{-arg})$, although noisier, this spectrum is not significantly different from the other two. Relative signal intensity within each spectrum is indicated by color from blue through red which is the maximum intensity in each displayed spectrum.

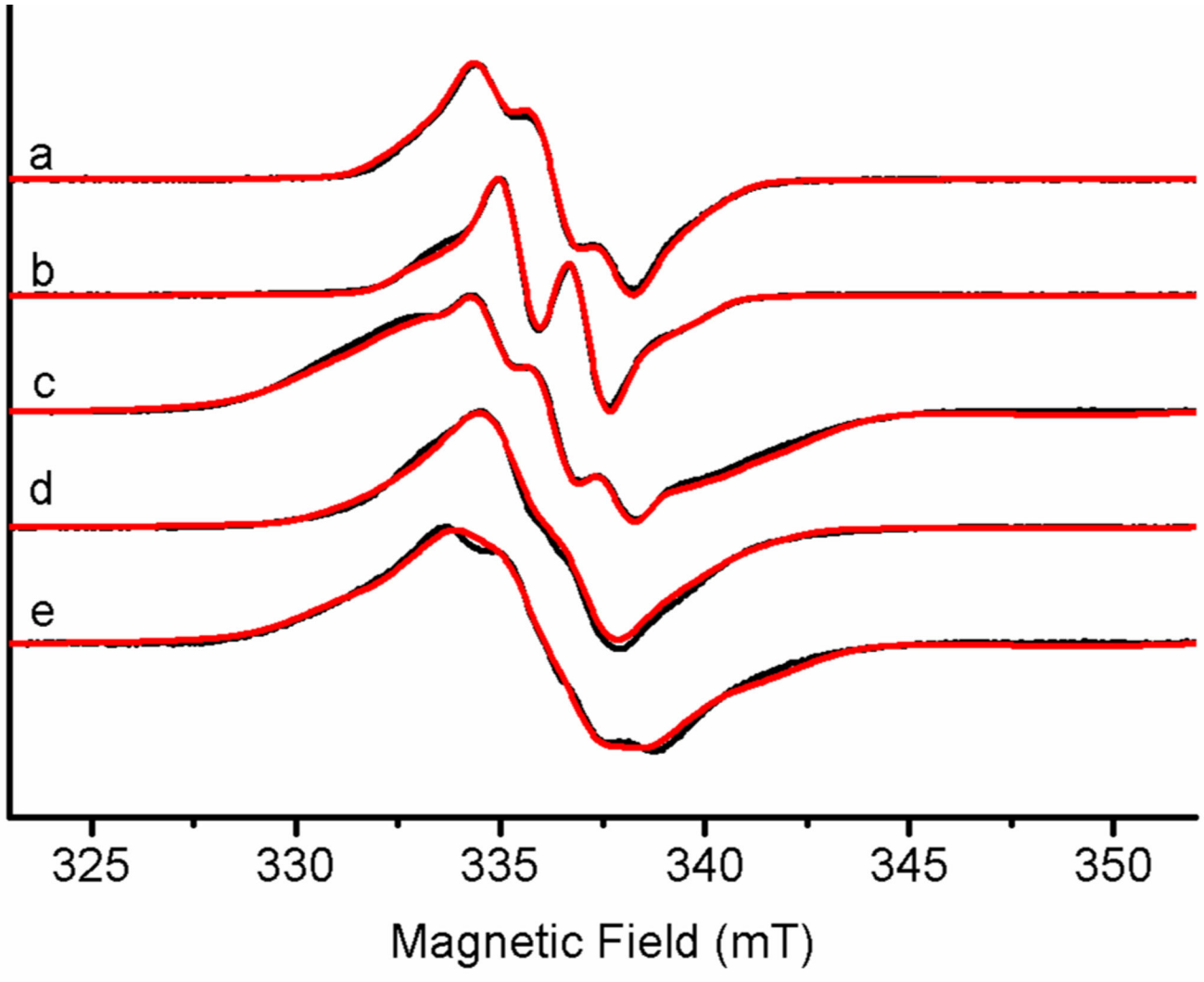


**Figure 5.**

CW-EPR spectra of the free radicals. (a) $nNOS_{FQ}$(+$BH_4$, +L-arg) in $H_2O$, (b) $nNOS_{FQ}$(+$BH_4$, +L-arg) in $D_2O$, (c) $nNOS_{FQ}$(+$BH_4$, - L-arg) in $H_2O$, (d) $nNOS_{FQ}$(+$BH_4$, - L-arg) in $D_2O$ and (e) $nNOS_{FQ}$(+$BH_4$, −L-arg) with $^{15}N$ at N5 of $BH_4$ in $H_2O$. The black curves are the experimental spectra and the red curves are simulations by EasySpin using the hyperfine parameters in Table 2 (scaled for $^{2}H$ or $^{15}N$ as needed). The simulated spectra in (a–b) do not include any spin coupling to heme while spectra (c–e) are the sum of simulated spectra with and without spin coupling to the heme, as described in the text. The experimental spectra were measured at 77 K and 9.437 GHz with 8.35 mW microwave power and 0.5 mT modulation amplitude at 100 kHz.

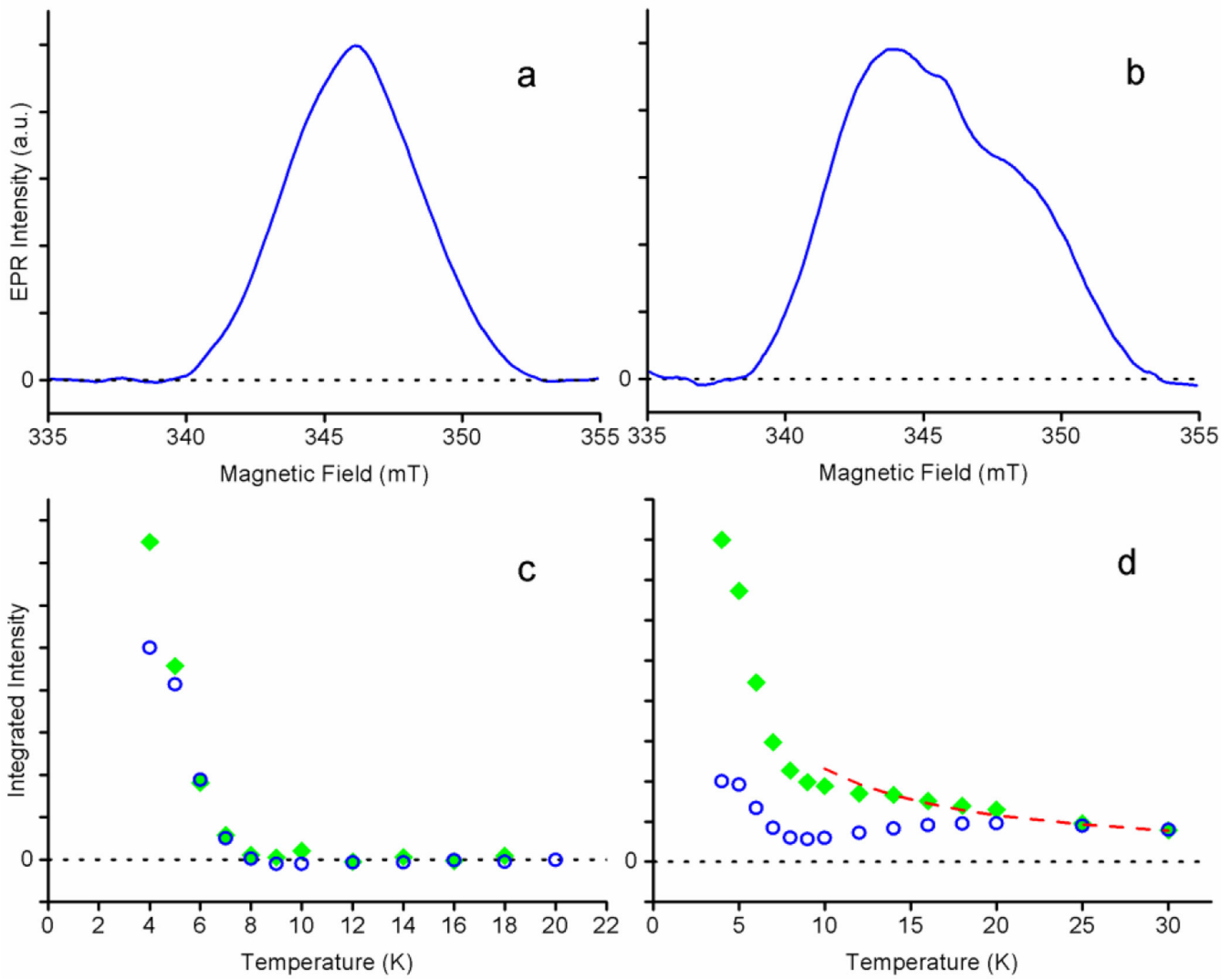


**Figure 6.**

The two-pulse ED-EPR free radical spectra and intensities. A 0.1 kHz pulse repetition rate was used for (a) $nNOS_{FQ}(+BH_4, +L\text{-arg})$ at 4 K and (b) $nNOS_{FQ}(+BH_4, -L\text{-arg})$ at 18 K. The integral of the ED-EPR spectrum between 342.0 and 349.0 mT as a function of temperature at repetition rates of 2 kHz (open blue circles) and 0.1 kHz (filled green diamonds) for (c) $nNOS_{FQ}(+BH_4, +L\text{-arg})$ and (d) $nNOS_{FQ}(+BH_4, -L\text{-arg})$ at 9.74 GHz and $\tau$=160 ns. The signal intensity represented by the open blue circles in (d) increases between 10–20 K as the $1/T_{1e}$ of the slow-relaxing radical becomes comparable to the 2 kHz repetition rate.

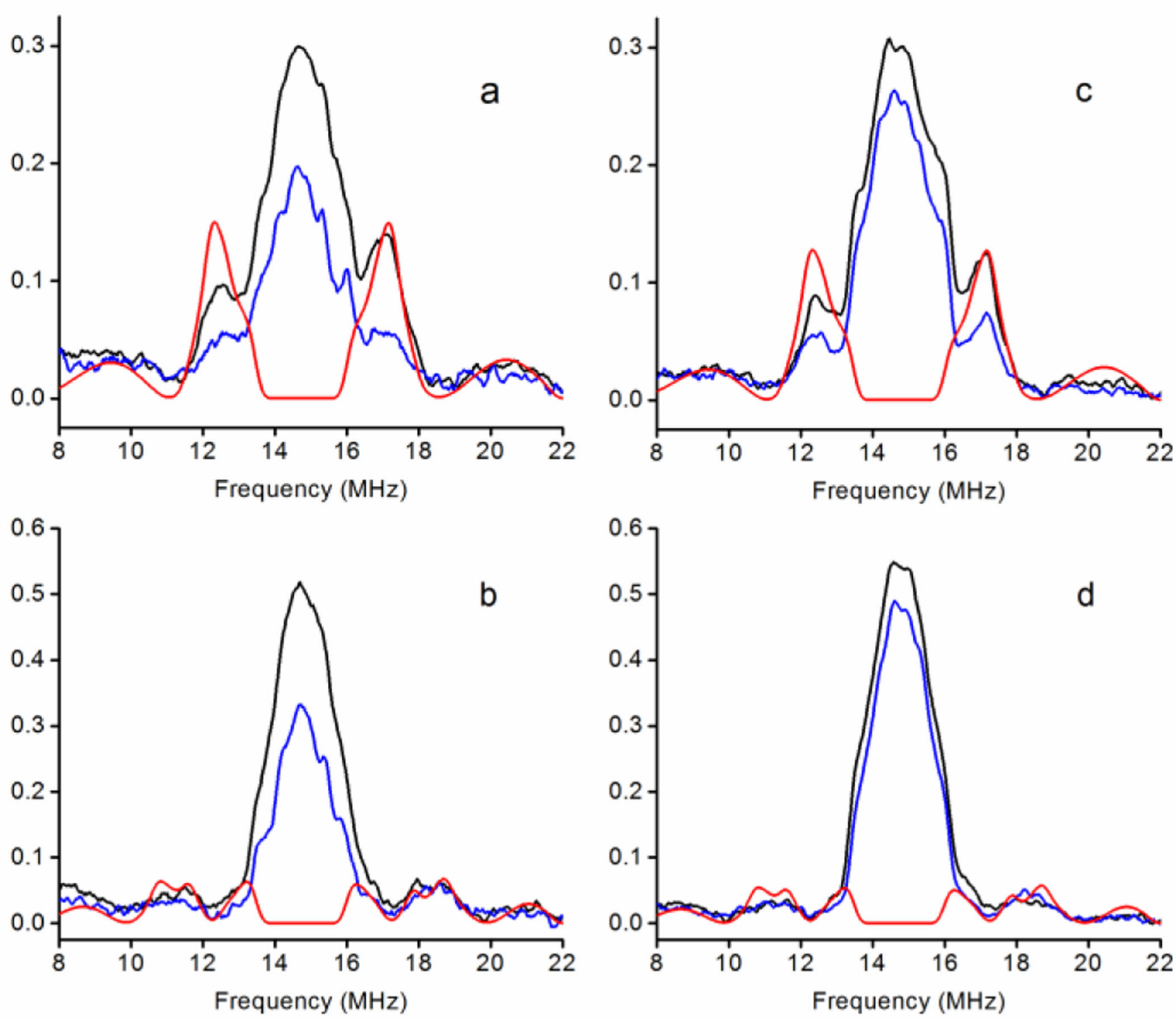


**Figure 7.**

Mims ENDOR spectra of the free radicals. (a–b) $nNOS_{FQ}$(+$BH_4$, +L-arg) at 4 K and (c–d) $nNOS_{FQ}$(+$BH_4$, −L-arg) at 10 K measured using (a, c) **τ**=132 ns and (b, d) **τ**=200 ns. The black lines are experimental spectra in $H_2O$, the blue lines are experimental spectra in $D_2O$ and the red lines are simulations of $^1H$ at C7 and N8 using parameters in Table 2. The intense matrix line near 15 MHz arises from a multitude of $^1H$ of water and the protein near the radical. The experimental spectra were measured at 9.725 GHz and 346 mT with an RF **π** pulse length of 10 μs and are plotted as the absolute ENDOR effect. Mims ENDOR blindspots appear as minima in the spectra near 11.2 and 18.7 MHz in (a, c) and near 9.8, 12.2, 17.2 and 19.7 MHz in (b, d).

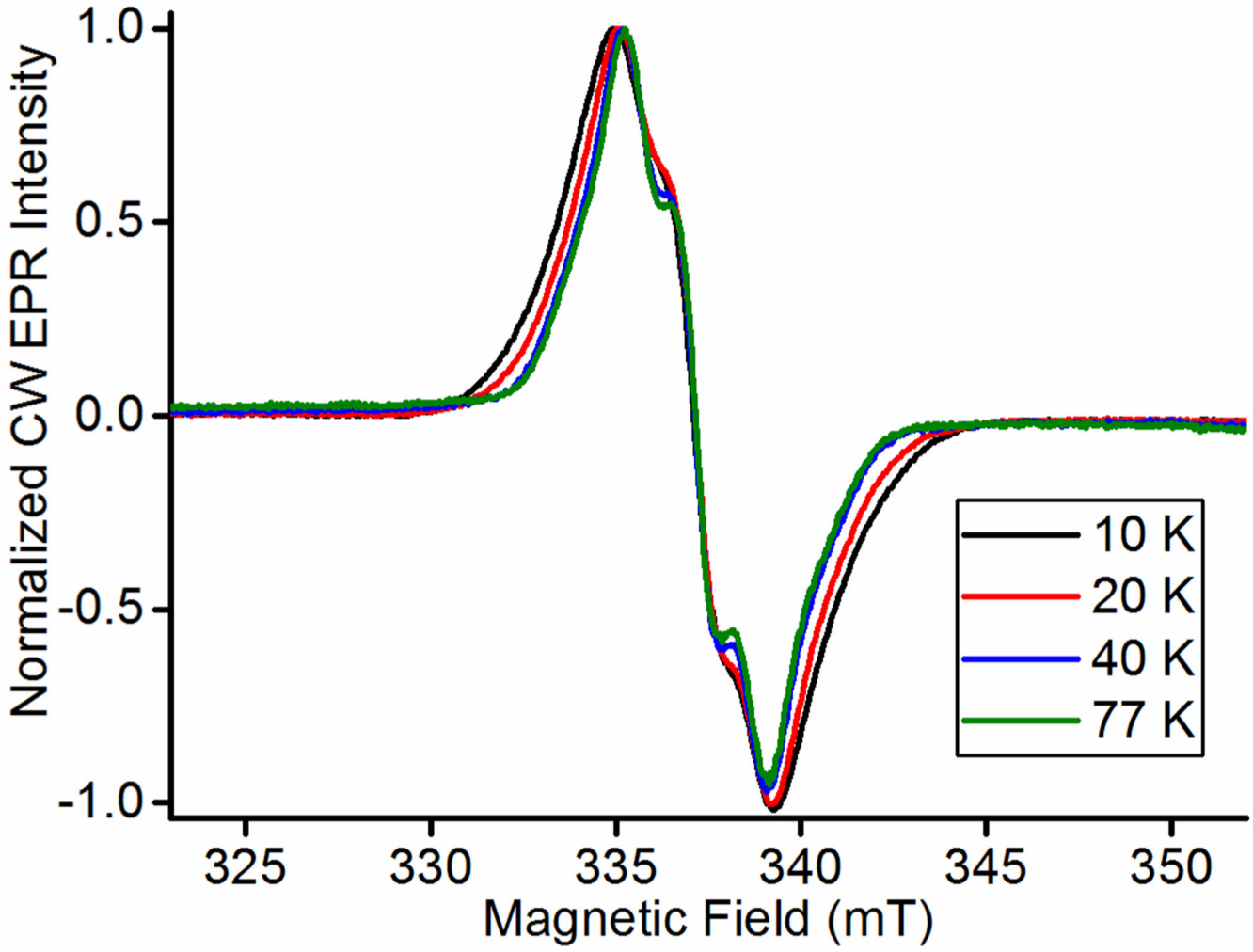


**Figure 8.**

The CW EPR spectra of the narrow free radical in $nNOS_{FQ}$(+$BH_4$, +L-arg) from 10–77 K and 9.437 GHz with 8.35 mW microwave power and 0.5 mT modulation amplitude at 100 kHz. Measurement temperatures -- cyan: 10 K; red: 20K; yellow: 40 K; purple: 77K.

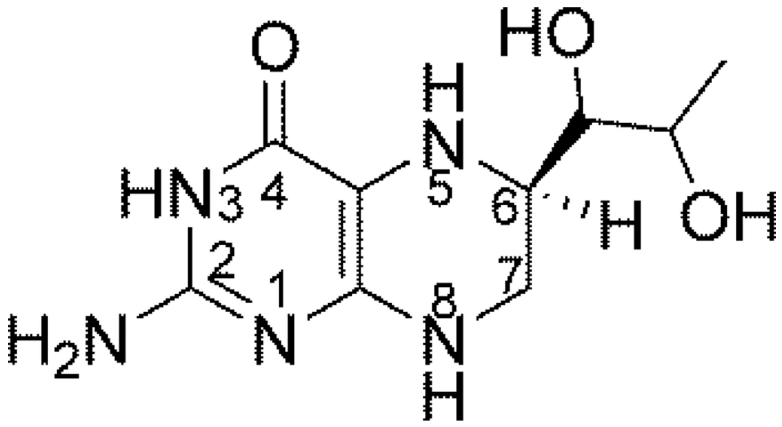


**Scheme 1.**
Structure of $BH_4$.

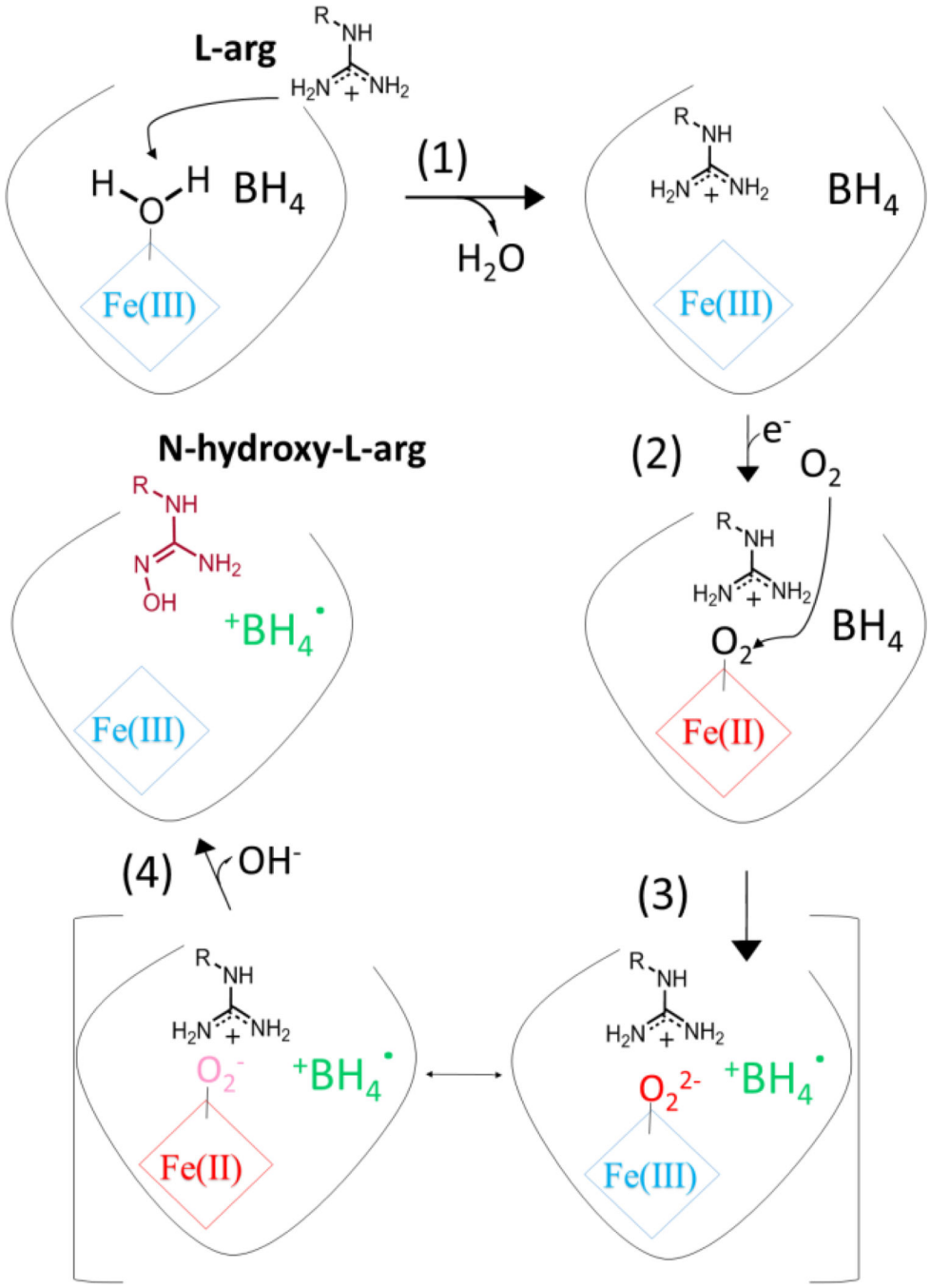


**Scheme 2.**

The first mono-oxygenation reaction cycle in $NOS_{OX}$ with key steps numbered. The resting state of the enzyme in the upper, left-hand corner has a hexa-coordinate (Fe(III) heme) with an axial water ligand. Its EPR spectrum has g-factors between ~1.8–2.6, typical of a low-spin (Fe(III) heme)-thiolate [9]. After L-arg binding in step 1 and at the end of the first cycle after step 4, there is no axial water ligand and the penta-coordinate (Fe(III) heme)-thiolate has an EPR spectrum with g-factors spanning the 1.8–8.0 range typical of high-spin heme. Other (Fe(III) heme) intermediates in this scheme (and similar states in side reactions) have

lifetimes much shorter than the reaction times in the RFQ experiments and are not be present in our samples.

**Table 1**

Heme EPR Parameters and Spectral Weights from least-squares fits of spectra using EasySpin

| **Species** | **Low-Spin Heme** | | | **High-Spin Heme** | |
|---|---|---|---|---|---|
| EPR Spectral Parameters | $g_x$ =1.881<br>$g_y$ =2.290<br>$g_z$ =2.434 | $g_x$ =1.892<br>$g_y$ =2.275<br>$g_z$ =2.468 | $g_x$ =1.912<br>$g_y$ =2.286<br>$g_z$ =2.41 | D =8.2 $cm^{-1}$<br>E/D =0.081<br>g =2.03 | D =8.2 $cm^{-1}$<br>E/D =0.071<br>g =2.03 |
| $nNOS_{OX}$(−$BH_4$, −L-arg) | 22% | 44% | 25% | 7% | 2% |
| $nNOS_{OX}$(−$BH_4$, +L-arg) | 2% | 15% | 12% | 56% | 15% |
| $nNOS_{FQ}$(+$BH_4$, +L-arg) | 0% | 3% | 2% | 68% | 27% |
| $nNOS_{FQ}$(+$BH_4$, −L-arg) | 33% | 32% | 12% | 19% | 4% |

**Table 2**

$BH_4$ radical cation hyperfine tensors following the notation of Stoll et al. [15]. These hyperfine tensors are derived from fits by EasySpin of the CW-EPR and ENDOR spectra with coincident g and hyperfine tensor axes.

| Nucleus | Assigned Position | Hyperfine Tensor (MHz) |
|---|---|---|
| $^{1}H$ exchangeable | N5 | [−12, −52, −27] |
| $^{14}N$ | N5 | [0, 0, 64] |
| $^{1}H$ | C6 | [46, 46, 44] |
| $^{1}H$ | C7 (tentative) | [4.0, 14.0, 8.0] |
| $^{1}H$ exchangeable | N8 (tentative) | [2.5, 5, 6.5] |